Irrigation-driven land subsidence on the Barind Tract, northwest Bangladesh: two-track Sentinel-1 InSAR, GNSS-tied time series and spatially cross-validated explainable machine learning

Farheen Zaman[1,*] and Ashfaq Raveed[2]

[1]Department of Petroleum and Mining Engineering, Shahjalal University of Science and Technology, Sylhet 3114, Bangladesh
[2]Department of Mechanical Engineering, Bangladesh University of Engineering and Technology, Dhaka 1000, Bangladesh

[*]Corresponding author: zamanfarheen5@gmail.com
Ashfaq Raveed: ashfaqraveed7@gmail.com

This manuscript is a **non-peer-reviewed preprint** submitted to EarthArXiv.
It has not yet undergone peer review or been accepted for publication in a journal.
Subsequent versions of this manuscript may have slightly different content.
Please feel free to contact the corresponding author with feedback.

Irrigation-driven land subsidence on the Barind Tract, northwest Bangladesh: two-track Sentinel-1 InSAR, GNSS-tied time series and spatially cross-validated explainable machine learning

Farheen Zaman[a,*], Ashfaq Raveed[b]

[a]*Department of Petroleum and Mining Engineering, Shahjalal University of Science and Technology, Sylhet, 3114, Bangladesh*
[b]*Department of Mechanical Engineering, Bangladesh University of Engineering and Technology, Dhaka, 1000, Bangladesh*

Abstract

The Barind Tract of northwest Bangladesh is the country's most intensively groundwater-irrigated region, yet its ground motion has been measured only at isolated points. We processed ascending and descending Sentinel-1 small-baseline InSAR networks for 2017–2025, referenced them to a continuous GNSS station and converted line-of-sight rates to vertical velocity. In the ascending track, coherent land subsides at a median of -10.1 mm yr^{-1} (median formal uncertainty 0.58 mm yr^{-1}, plus a common ± 1.7 mm yr^{-1} GNSS-tie uncertainty), and 51% of it subsides faster than 10 mm yr^{-1}. Rates reach -11.2 ± 1.2 mm yr^{-1} at Godagari on the Barind margin, against -1.8 ± 1.1 mm yr^{-1} on the active Ganges floodplain; 1-km block medians from the two tracks correlate at $r = 0.56$. GLDAS-2.2 groundwater storage declined by 7.2 ± 1.2 mm yr^{-1}, and the fitted seasonal ground low lags the April storage minimum by three to four months, consistent with delayed aquitard drainage. An ERA5 tropospheric correction changed velocities by a median of 0.03 mm yr^{-1} and shifted this timing by at most three weeks at three of four sites. Random forest and XGBoost models explain 37–47% of the spatial variance under 5-km spatial block cross-validation; random cross-validation inflates R^2 by 0.09–0.13, and omitting ramp removal raises it to 0.69. SHAP effects with

*Corresponding author
Email addresses: zamanfarheen5@gmail.com (Farheen Zaman), ashfaqraveed7@gmail.com (Ashfaq Raveed)

the same direction in both tracks identify elevation, built-up density and local Boro irrigation intensity as robust controls. Subsidence removes at least 25 million m^3 of ground volume per year, of the same order as the groundwater-storage decline, and 601 km of main roads and 101 km of railway lie on ground subsiding faster than 10 mm yr^{-1}. Spatial cross-validation and cross-track consistency should precede physical interpretation of machine-learning attributions of subsidence.

Keywords: Land subsidence, InSAR, Groundwater irrigation, Barind Tract, Explainable machine learning, Spatial cross-validation

1. Introduction

Land subsidence caused by groundwater abstraction affects aquifer systems on every inhabited continent and threatens infrastructure, flood protection and the long-term storage capacity of aquifers (Galloway and Burbey, 2011; Herrera-García et al., 2021; Bagheri-Gavkosh et al., 2021). Global syntheses estimate that a large fraction of the world's population lives in areas susceptible to subsidence and that compaction of fine-grained layers has permanently reduced aquifer storage in many over-exploited basins (Hasan et al., 2023; Davydzenka et al., 2024). Recent national-scale InSAR inventories show that subsidence is not only a coastal-megacity problem but also affects agricultural and inland urban regions (Ao et al., 2024; Ohenhen et al., 2024).

Bangladesh occupies most of the Ganges–Brahmaputra–Meghna (GBM) delta, one of the most populous and most vulnerable deltas on Earth (Syvitski et al., 2009; Tessler et al., 2015). Subsidence in the delta has been studied with stratigraphy, tide gauges, GNSS and InSAR, but almost exclusively in the young Holocene delta plain and the coastal zone (Higgins et al., 2014; Brown and Nicholls, 2015; Grall et al., 2018; Becker et al., 2020; Steckler et al., 2022). In contrast, the Barind Tract, an uplifted Pleistocene terrace in northwest Bangladesh (Morgan and McIntire, 1959; Brammer, 2012), has received little geodetic attention, even though it is the part of the country where dry-season (Boro) rice irrigation has most strongly depleted groundwater (Jahan et al., 2010; Rahman and Mahbub, 2012; Dey et al., 2017; Mojid et al., 2019). Long-term water-level declines of several metres in the Barind upazilas are well documented by monitoring wells. Recent Sentinel-1 studies report a line-of-sight subsidence rate of about 8 mm yr^{-1} at a single Rajshahi site (Middleton et al., 2025) and a national-scale correspondence between GRACE groundwater storage and InSAR subsidence (Ouyang et al., 2024), but the spatial pattern of subsidence across the Barind Tract, its vertical

rate in an absolute reference frame and its geological and land-use controls remain unknown.

At the same time, studies that attribute subsidence to its drivers increasingly use machine learning (ML) with remote-sensing predictors (Mohammady et al., 2019; Shi et al., 2020; Smith and Majumdar, 2020). These models are usually validated with random train–test splits, although InSAR velocities are strongly spatially autocorrelated, so random splits leak information and overstate predictive skill (Roberts et al., 2017; Ploton et al., 2020; Meyer and Pebesma, 2021). Feature-importance statements from such models are also rarely tested for robustness to the satellite viewing geometry or to processing choices.

To place this study in context, we reviewed the literature systematically, following the PRISMA 2020 reporting guideline (Page et al., 2021). Scopus was searched on 7 November 2026 (field `TITLE-ABS-KEY`) for English-language articles and reviews published between 2000 and 2025, using three query blocks combined with `OR` inside and `AND` between blocks:

1. *process*: `"land subsidence" OR "ground subsidence" OR "aquifer compaction" OR "aquitard"`;
2. *method*: `InSAR OR "SAR interferometry" OR "persistent scatterer" OR "small baseline" OR GNSS OR "machine learning" OR "random forest" OR XGBoost OR SHAP`;
3. *setting*: `Bangladesh OR "Bengal Basin" OR "Ganges-Brahmaputra" OR Barind OR "groundwater irrigation" OR "groundwater depletion"`.

Studies were included if they (a) measured or modelled land subsidence or groundwater-storage change associated with groundwater abstraction, or (b) used statistical or ML models to explain the spatial pattern of subsidence. Titles and abstracts of all records were screened by the authors. Because the query requires a subsidence term, purely hydrological studies of the Bengal Basin and several method papers were not retrieved; these were added by backward snowballing from the reference lists of included papers. The search returned 72 records; three were excluded (groundwater arsenic, mining-induced deformation, and a compilation of aquitard parameters without subsidence or storage measurements), leaving 69. Snowballing added 31 studies, giving 100 studies in the synthesis (Fig. 1). All screened records, with region, methods and screening decision, are listed in Table S1. Of the 69 database records, 60 used InSAR, 20 combined InSAR or subsidence data with GRACE, and only six used ML or statistical attribution; eight concerned Bangladesh. The studies most relevant to this work are summarised in Table 1.

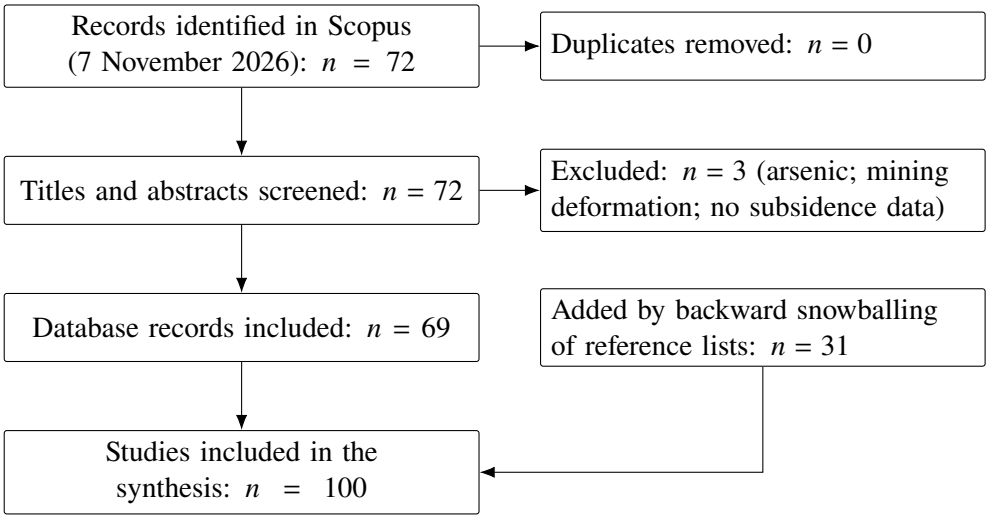


Figure 1: PRISMA 2020 flow diagram of the literature search and screening.

Geological subsidence of the GBM delta is driven by sediment loading, compaction of Holocene muds and tectonic flexure of the Bengal Basin (Goodbred and Kuehl, 2000; Grall et al., 2018). Holocene-averaged rates derived from dated stratigraphy are typically a few mm yr^{-1}, with higher values in the subsiding Sylhet basin and the lower delta plain (Grall et al., 2018; Steckler et al., 2022). Present-day rates measured with GNSS, tide gauges and InSAR are more variable. The first InSAR study of the delta used ALOS PALSAR L-band data for 2007–2011 and found rates of 0–18 mm yr^{-1} around Dhaka and the lower delta, concentrated on young Holocene sediments and partly attributed to shallow compaction and groundwater pumping (Higgins et al., 2014). Water-level and GNSS records along the coast indicate that relative sea-level rise in the delta is dominated by land subsidence rather than ocean rise (Becker et al., 2020). A synthesis of all available measurements concluded that subsidence of the lower delta is spatially heterogeneous, generally 2–10 mm yr^{-1}, and controlled mainly by the thickness of compressible Holocene sediment (Steckler et al., 2022). Human influences, including groundwater abstraction, sediment starvation behind embankments and drainage, are recognised as accelerating factors (Brown and Nicholls, 2015; Syvitski et al., 2009). None of these studies cover the Pleistocene Barind Tract, where Holocene deposits are thin or absent and a different mechanism — compaction of the clay-rich Barind residuum and underlying aquitards by deep pumping — would be expected.

Eight of the database records concern Bangladesh, and all but two were published since 2024. Campaign GNSS resurveys of coastal monuments show rates from below 2 mm yr^{-1} on thin, sandy Holocene interfluves to 20–25 mm yr^{-1} where Holocene muds are thick (Steckler et al., 2024). Sentinel-1 InSAR in southwestern Bangladesh gives mostly 3–10 mm yr^{-1}, locally up to 20 mm yr^{-1} (Sarker et al., 2024); in Dhaka, ALOS and Sentinel-1 reveal widespread subsidence above 10 mm yr^{-1} that accelerated to more than 50 mm yr^{-1} in newly reclaimed wetlands and correlates with groundwater levels (Khan and Xie, 2025); and two-track SBAS along the Dhaka–Gopalganj railway shows quasi-vertical subsidence of about 16 mm yr^{-1}, highest on crop land and deltaic silt (Kyaw and Takeuchi, 2025). Only two studies reach the northwest. Middleton et al. (2025) analysed ascending Sentinel-1 data for five target sites and reported line-of-sight rates of 8 mm yr^{-1} at Rajshahi, without a GNSS tie or a vertical conversion. Ouyang et al. (2024) combined GRACE/GLDAS groundwater storage with national-scale SBAS-InSAR, found the strongest storage declines in Rangpur, Mymensingh and Rajshahi, and reported that subsidence lags groundwater storage by 2–6 months. Neither study maps the Barind Tract at a resolution that resolves its geological units, uses independent viewing geometries, or attributes the spatial pattern to its drivers.

Since the 1980s, northwest Bangladesh has changed from rain-fed agriculture to irrigated dry-season Boro rice supplied mainly by shallow and deep tube wells (Qureshi et al., 2015). Hydrograph analyses show that the dry-season water table is falling across much of the northwest and that in the Barind Tract many shallow wells no longer reach water in the dry season (Shamsudduha et al., 2009; Jahan et al., 2010; Rahman and Mahbub, 2012; Mojid et al., 2019). Abstraction has increased recharge in parts of the Bengal Basin (Shamsudduha et al., 2011), but recharge on the Barind clays is limited by low-permeability surface soils, so storage losses accumulate (Dey et al., 2017; Mojid et al., 2019). At the regional scale, GRACE gravimetry has been validated against well-based storage changes in the Bengal Basin (Shamsudduha et al., 2012) and shows a long-term decline in total water storage across the Indo–Gangetic aquifer system (Rodell et al., 2009, 2018). These hydrological studies document the forcing that could cause aquifer compaction, but none measure the ground-surface response.

Multi-temporal InSAR, using persistent scatterers (Ferretti et al., 2001) or small-baseline subsets (Berardino et al., 2002), has become the standard tool for mapping groundwater-induced subsidence. In alluvial basins, InSAR time series reveal both a long-term inelastic component, from compaction of clay interbeds, and a seasonal elastic component that follows hydraulic head (Chaussard

et al., 2014; Smith et al., 2017; Haghshenas Haghighi and Motagh, 2019). The lag between head change and surface response reflects slow drainage of thick aquitards, so the seasonal timing of InSAR displacement is itself diagnostic of the compacting layers (Galloway and Burbey, 2011; Smith et al., 2017). Combining InSAR with GRACE allows regional storage losses to be separated into recoverable and permanent components (Castellazzi et al., 2016; Ojha et al., 2018; Hasan et al., 2023); 20 of the 69 database records used this combination. Comparable studies in Asian deltas show subsidence of several centimetres per year where groundwater extraction is intense (Chaussard et al., 2013; Erban et al., 2014; Minderhoud et al., 2017), and in the adjacent Indian Ganga plain InSAR links subsidence of up to several centimetres per year around Delhi and Lucknow to groundwater over-extraction (Kumar et al., 2022; Raju et al., 2022; More et al., 2025). Free Sentinel-1 data (Torres et al., 2012) and open processing services such as HyP3 (Alaska Satellite Facility, 2025) and MintPy (Yunjun et al., 2019) now make such analyses feasible for data-poor regions, but tying InSAR to an absolute reference frame still requires GNSS (Blewitt et al., 2018), and separating vertical from horizontal motion requires more than one viewing geometry (Wright et al., 2004; Fuhrmann and Garthwaite, 2019).

Data-driven studies have used random forests, boosted trees and neural networks to map subsidence susceptibility or predict InSAR velocities from hydrogeological, land-use and climatic predictors (Mohammady et al., 2019; Shi et al., 2020; Smith and Majumdar, 2020; Zhao et al., 2024; Huang et al., 2025; Davydzenka et al., 2024; Hasan et al., 2023). Tree ensembles (Breiman, 2001; Chen and Guestrin, 2016) capture nonlinear and interacting effects, and Shapley-value methods (Lundberg and Lee, 2017; Lundberg et al., 2020) make their predictions interpretable at the level of individual pixels. Three weaknesses recur in this literature (Table 1); only six of the 69 database records used any ML or statistical attribution. First, most studies validate with random splits of spatially autocorrelated pixels or with a random 70/30 hold-out of inventory points (Zhao et al., 2024), which inflates reported skill (Roberts et al., 2017; Ploton et al., 2020; Valavi et al., 2019). Second, explanations are rarely checked for stability, for example across independent satellite geometries or processing variants. Third, susceptibility studies often use subsidence inventories without a vertical reference frame, so the target variable itself can contain orbital or atmospheric artefacts.

Together, the literature shows four gaps: (1) InSAR studies in Bangladesh concentrate on Dhaka, the coast and a few point locations, and no spatially complete, GNSS-tied vertical velocity map exists for the Barind Tract despite its documented groundwater depletion; (2) the lag between groundwater storage and ground mo-

tion has been reported only at national scale (Ouyang et al., 2024) and has not been resolved spatially or related to geology; (3) ML attributions of subsidence are rarely validated with spatial cross-validation; and (4) explanations are seldom tested for robustness across viewing geometries.

This study addresses these gaps. Our objectives are to: (i) produce the first GNSS-tied, two-track Sentinel-1 InSAR vertical velocity field and time series for the Barind Tract and adjacent floodplains; (ii) relate ground motion to regional groundwater-storage change and its seasonal timing; and (iii) attribute the spatial pattern of subsidence to irrigation, geology, terrain, urbanisation and soils with spatially cross-validated random forest and XGBoost models interpreted with SHAP, keeping only attributions that are consistent between the ascending and descending tracks.

2. Study area

The study area is the part of Rajshahi Division covered by the ascending frame, about 140 × 70 km between 88.0–89.4°E and 24.2–24.9°N (Fig. 2). It includes the western part of the Barind Tract, the Ganges (Padma) floodplain to the south and the Atrai–Little Jamuna floodplains to the east. The Barind Tract is an uplifted Pleistocene terrace, 10–45 m above sea level, capped by the oxidised Barind clay residuum and dissected by fault-guided valleys (Morgan and McIntire, 1959; Brammer, 2012). Mapped geological units (Persits et al., 2001) are Barind clay residuum (rb), alluvial silt and clay (asc), alluvial silt (asl), marsh clay and peat (ppc) and alluvial sand (asd) (Fig. 2b). The climate is monsoonal, with most rainfall from June to September and a dry season from November to May. Boro rice, transplanted in January–February and harvested in April–May, is irrigated almost entirely from groundwater (Qureshi et al., 2015; Dey et al., 2017). Rajshahi city, the largest urban area, hosts the RAJS continuous GNSS station used as the geodetic reference.

3. Data and methods

The workflow is summarised in Fig. 3. All data are open; all processing code is available (see Data availability).

3.1. Sentinel-1 InSAR processing

We used Sentinel-1 interferometric wide-swath acquisitions (Torres et al., 2012) from ascending path 12 (March 2017–December 2025) and descending

Table 1: Summary of key studies from the systematic review, grouped by theme.

Study	Region	Data / method	Main finding and limitation relevant here
Subsidence in the GBM delta			
Higgins et al. (2014)	Bangladesh delta	ALOS PALSAR SBAS, 2007–2011	0–18 mm yr^{-1} on Holocene sediments; no coverage of the Barind; L-band, no GNSS tie
Grall et al. (2018)	Lower delta	Dated stratigraphy	Holocene-averaged subsidence of a few mm yr^{-1}; geological, not present-day
Becker et al. (2020)	Coastal GBM	Tide gauges, GNSS, altimetry	Relative sea-level rise dominated by subsidence; coastal only
Steckler et al. (2022)	Lower GBM	Synthesis of all methods	2–10 mm yr^{-1} controlled by Holocene thickness; Pleistocene terraces unstudied
Steckler et al. (2024)	Coastal Bangladesh	Campaign GNSS	<2 to 25 mm yr^{-1}, increasing with Holocene mud thickness
Recent InSAR in Bangladesh			
Sarker et al. (2024)	SW Bangladesh	Sentinel-1 InSAR	Mostly 3–10 mm yr^{-1}; coastal floodplain only
Khan and Xie (2025)	Dhaka	ALOS + Sentinel-1	>10 mm yr^{-1}, accelerating on reclaimed wetland; urban only
Kyaw and Takeuchi (2025)	Dhaka–Gopalganj	Two-track SBAS	$\approx$16 mm yr^{-1} along a railway corridor
Middleton et al. (2025)	N and central Bangladesh	Ascending Sentinel-1 DInSAR/PSI	8 mm yr^{-1} LOS at Rajshahi; five point sites, no GNSS tie
Ouyang et al. (2024)	Bangladesh	GRACE/GLDAS + SBAS	2–6 month lag of subsidence behind storage; national scale
Groundwater depletion			
Shamsudduha et al. (2009)	Bangladesh	Well hydrographs, trend tests	Falling dry-season heads in the northwest
Rahman and Mahbub (2012); Jahan et al. (2010)	Barind Tract	Wells, irrigation records	Water table decline linked to deep tubewell irrigation; no ground-motion data
Mojid et al. (2019)	NW Bangladesh	Well trends	Widespread unsustainable decline
InSAR and aquifer compaction elsewhere			
Chaussard et al. (2014)	Central Mexico	ALOS SBAS	Subsidence follows clay-rich basin fill
Smith et al. (2017)	San Joaquin Valley	InSAR + heads	Seasonal elastic vs long-term inelastic compaction; aquitard delay
Machine-learning attribution			
Mohammady et al. (2019)	Iran	RF susceptibility	Random validation; categorical inventory target
Shi et al. (2020)	Beijing	ML on InSAR	Multi-factor prediction; random validation
Smith and Majumdar (2020)	Western USA	RF on InSAR	Storage loss mapped from ML; regional scale
Zhao et al. (2024)	Not stated	Hybrid tree classifiers	AUC 0.98 on 94 inventory points; random 70/30 hold-out
Huang et al. (2025)	North China Plain	Geodetector on SBAS + GRACE	Storage anomaly strongest factor; lagged response to deep pumping
Davydzenka et al. (2024)	Global	ML on InSAR compilations	Global susceptibility map; coarse resolution

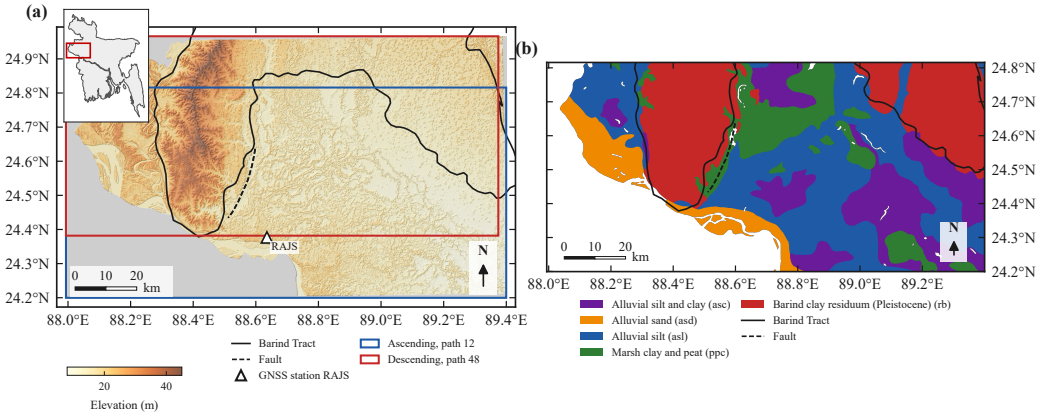


Figure 2: Study area. (a) Elevation (hillshaded) with the Barind Tract outline, mapped fault, the processed ascending (path 12) and descending (path 48) Sentinel-1 areas and the RAJS GNSS station; inset shows the location in Bangladesh. (b) Surface geology (Persits et al., 2001).

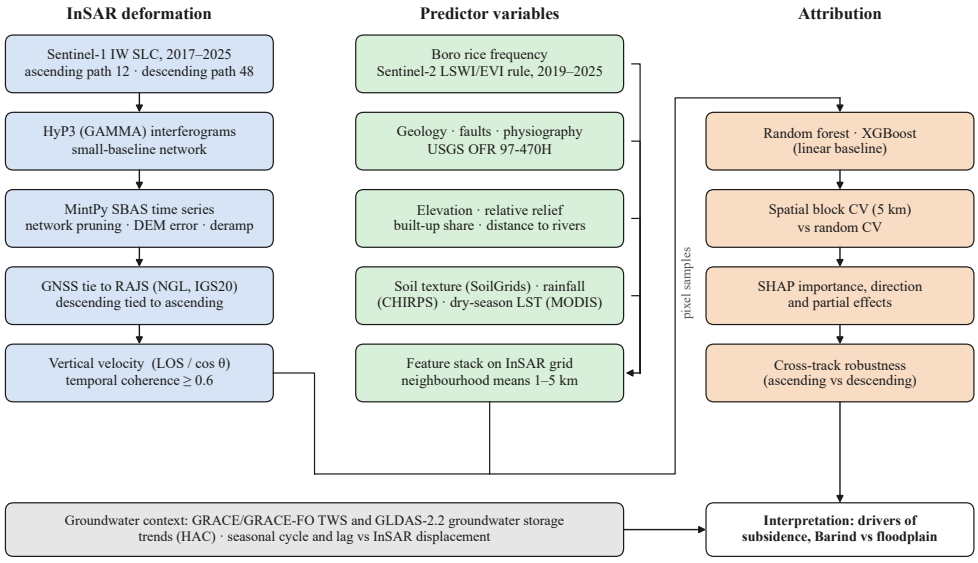


Figure 3: Workflow of InSAR processing, predictor preparation, attribution modelling and groundwater analysis.

path 48 (January 2017–December 2024). Interferograms were generated with the HyP3 GAMMA on-demand service (Alaska Satellite Facility, 2025) at 80 m posting for a small-baseline network that connects each acquisition to its nearest neighbours in time. Time series were inverted with MintPy (Yunjun et al., 2019) using the small-baseline approach (Berardino et al., 2002) with ordinary least squares and no weighting. Acquisitions that would leave the network poorly connected, or that were dominated by decorrelation, were excluded: 10 of 269 ascending and 20 of 222 descending dates were removed, leaving 704 of 735 and 530 of 617 interferograms, respectively (Fig. S1). We corrected topographic residuals (Fattahi and Amelung, 2013) and removed a linear phase ramp from each epoch to suppress residual orbital and long-wavelength atmospheric signal. Velocity was estimated by linear regression of the time series, and pixels with temporal coherence below 0.6 were masked. Line-of-sight (LOS) velocity was converted to vertical velocity as $v_U = v_{\mathrm{LOS}}/\cos\theta$, where θ is the local incidence angle, assuming negligible horizontal motion. Areas outside Bangladesh were masked.

3.2. GNSS reference frame and two-track consistency

The ascending velocity field was referenced to a window around RAJS and shifted so that its vertical velocity equals the RAJS vertical rate from the Nevada Geodetic Laboratory IGS20 solution, -3.10 ± 1.69 mm yr^{-1} (Blewitt et al., 2018). This uniform shift carries the GNSS uncertainty into all absolute rates; relative rates are unaffected. Because RAJS lies outside the descending frame, the descending field was tied to the ascending field by fitting an offset and plane to their difference over common coherent pixels. Agreement between tracks was evaluated on 1-km block medians. Formal three-dimensional decomposition (Wright et al., 2004; Fuhrmann and Garthwaite, 2019) was tested, but with only two near-polar geometries the east component absorbs inter-track noise; we therefore used each track independently under the vertical-only assumption and treated their agreement as a test of that assumption.

3.3. Time-series and seasonal analysis

At four sites (Fig. 6a) we extracted the median vertical displacement of coherent pixels within 1 km, relative to a 500-m window at RAJS plus the RAJS GNSS rate. Each series was fitted with

$$d(t) = a + b\,t + \sum_{k=1}^{2} \left[c_k \cos(2\pi k t) + s_k \sin(2\pi k t)\right] + \varepsilon(t), \tag{1}$$

with Newey–West heteroscedasticity- and autocorrelation-consistent standard errors (Newey and West, 1987). The same model applied to every coherent pixel gave maps of seasonal amplitude and month of the seasonal low (Fig. S6). To test the sensitivity of velocities and seasonal timing to tropospheric delay, the time series was recomputed with and without an ERA5-based correction (PyAPS; Jolivet et al. 2011) for the 171 epochs (March 2017 to April 2024) for which ERA5 fields were available, using otherwise identical processing.

3.4. Groundwater storage

Regional water storage was characterised with JPL GRACE/GRACE-FO mascon total water storage (Tapley et al., 2004; Watkins et al., 2015; Landerer et al., 2020) and GLDAS-2.2 catchment land surface model groundwater storage, which assimilates GRACE (Li et al., 2019), averaged over the study area. Trends were estimated with Eq. (1) and checked with Sen's slope (Sen, 1968). The mean seasonal cycle of GLDAS groundwater storage over the InSAR period was compared with the mean harmonic seasonal cycle of InSAR displacement.

3.5. Predictor variables

Predictors (Table 2) were resampled to the InSAR grid in Google Earth Engine (Gorelick et al., 2017) and Python. Boro rice was mapped annually for 2019–2025 from Sentinel-2 (Drusch et al., 2012) with a phenology rule adapted from Xiao et al. (2005) and Dong and Xiao (2016): a flooding signal ($\mathrm{LSWI} + 0.05 \geq \mathrm{EVI}$) during January–February followed by a maximum $\mathrm{EVI} > 0.45$ between 10 March and 30 April. Boro frequency is the fraction of years a pixel was classified as Boro; neighbourhood means at 1, 3 and 5 km represent the density of surrounding pumping. District-total Boro areas from the 2022 Sentinel-2 map were compared with official 2021–22 district estimates (Bangladesh Bureau of Statistics, 2023) for the 20 districts overlapping the processing area (Fig. S3). The map reproduces the spatial pattern closely (Pearson $r = 0.91$, Spearman $\rho = 0.96$, $n = 20$) but underestimates the total area by 37%, as expected for a conservative phenology rule that rejects mixed, late-transplanted and cloud-obscured fields. Because the attribution models use Boro frequency as a relative index of irrigation intensity, this systematic underestimation does not affect the ranking of pixels.

3.6. Attribution models and validation

Up to 60 000 coherent pixels were sampled per track. We trained a linear baseline, random forest (Breiman, 2001) (300 trees, minimum leaf size 5) and XGBoost (Chen and Guestrin, 2016) (600 trees, depth 6, learning rate 0.05).

Table 2: Predictor variables used in the attribution models.

Predictor	Description	Source
Boro frequency	Fraction of 2019–2025 seasons mapped as Boro; pixel and 1, 3, 5 km means	Sentinel-2 (Drusch et al., 2012)
Geology	Five mapped surface units (one-hot encoded)	Persits et al. (2001)
Elevation, relative relief	DEM height; relief within 2 km	GEE DEM
Built-up share	Built-up fraction; pixel and 1, 3 km means	ESA WorldCover (Zanaga et al., 2021)
Distance to rivers	Distance to permanent surface water	JRC GSW (Pekel et al., 2016)
Clay, sand	Topsoil and 1–2 m clay and sand content	SoilGrids (Poggio et al., 2021)
Rainfall	Mean annual precipitation 2017–2025	CHIRPS (Funk et al., 2015)
Dry-season LST	Mean daytime land surface temperature	MODIS (Wan et al., 2015)

Performance was assessed with five-fold spatial block cross-validation using 5-km blocks (Roberts et al., 2017; Valavi et al., 2019) and, for comparison, with random five-fold cross-validation. Sensitivity runs changed the block size to 10 km, the coherence threshold to 0.5, removed redundant predictors (reduced model), used the descending track as target, and used the velocity field without ramp removal (Table 3). Residual spatial dependence was quantified with Moran's I (Moran, 1950) in distance bands up to 20 km.

Predictions of the final XGBoost models were explained with TreeSHAP (Lundberg et al., 2020). For each predictor we computed the mean absolute SHAP value and the Spearman correlation between predictor value and SHAP value, whose sign gives the direction of the effect. A predictor was considered a robust control only if the direction was the same in the ascending and descending models and $|\rho| > 0.1$ in both.

3.7. Volume loss and exposure

The annual volume lost to subsidence was computed as $V = \sum |v_U| A$ over coherent subsiding pixels of area A. Because long-term subsidence of compacting fine-grained layers is largely inelastic, V approximates the permanent loss of aquifer-system pore space (Smith et al., 2017; Hasan et al., 2023); it was compared

with the GLDAS groundwater-storage decline over the Bangladesh land in the frame. As V uses coherent pixels only, it is a lower bound for total subsidence volume; an upper estimate assumes that non-coherent land subsides at the coherent median. Exposure was quantified as the area of Boro cropland (Boro frequency ≥ 0.5) and built-up land (built-up share ≥ 0.5) and the length of national highways (OpenStreetMap motorway, trunk and primary), regional roads (secondary), district and feeder roads (tertiary) and railways (OpenStreetMap contributors, 2026) on ground subsiding faster than 10 mm yr^{-1}. Roads were sampled every 40 m and assigned the velocity of the nearest coherent pixel within 80 m.

4. Results

4.1. Vertical velocity field

Coherent pixels cover 2327 km^2 of Bangladesh territory in the ascending frame (Fig. 4). Subsidence dominates: the median vertical velocity is -10.1 mm yr^{-1} (interquartile range -14.8 to -6.0 mm yr^{-1}; 5th percentile -22.9 mm yr^{-1}). Subsidence exceeds 5 mm yr^{-1} over 80% and 20 mm yr^{-1} over 9% of the coherent area, and 51% of the coherent area subsides faster than 10 mm yr^{-1}. The fastest subsidence, locally exceeding 20 mm yr^{-1}, occurs on the western Barind Tract and its southern margin between Godagari and Tanore. The active Ganges floodplain south of Rajshahi is close to stable. Median velocity uncertainty from the MintPy regression is 0.58 mm yr^{-1} (95th percentile 0.88 mm yr^{-1}; Fig. S2), small compared with the signal; the uniform GNSS-tie uncertainty of ± 1.7 mm yr^{-1} dominates the error budget of absolute rates.

4.2. Agreement between tracks

The descending track reproduces the main pattern (Fig. 5). Over common coherent areas the 1-km block medians correlate with $r = 0.56$ ($n = 3835$) and scatter around the 1:1 line. Because the two geometries have opposite sensitivity to east–west motion, this agreement indicates that the signal is predominantly vertical, while the residual scatter bounds the combined effect of horizontal motion, atmospheric noise and the plane tie.

4.3. Time series and groundwater

All four sites subside steadily throughout 2017–2025 (Fig. 6). Rates are -11.2 ± 1.2 mm yr^{-1} at Godagari, -7.9 ± 0.6 mm yr^{-1} at Tanore and -5.7 ± 0.9 mm yr^{-1} at Nachole on the Barind Tract, and -1.8 ± 1.1 mm yr^{-1} at Charghat on the Ganges floodplain (uncertainties exclude the common GNSS-tie error). The series show

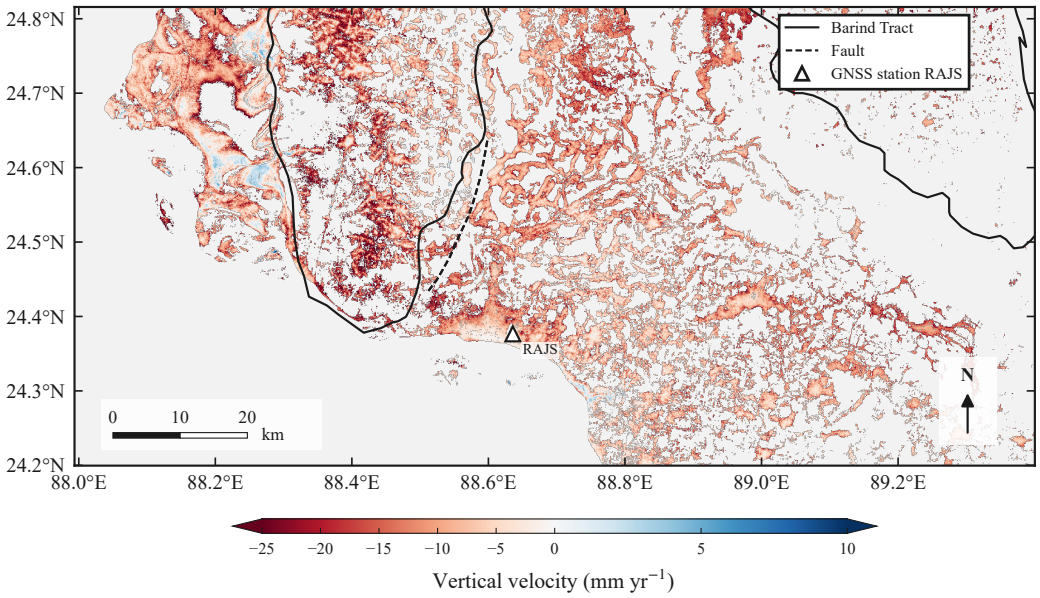


Figure 4: Ascending-track vertical velocity, 2017–2025, tied to the RAJS GNSS station. Grey: temporal coherence below 0.6 or outside Bangladesh. Negative values indicate subsidence.

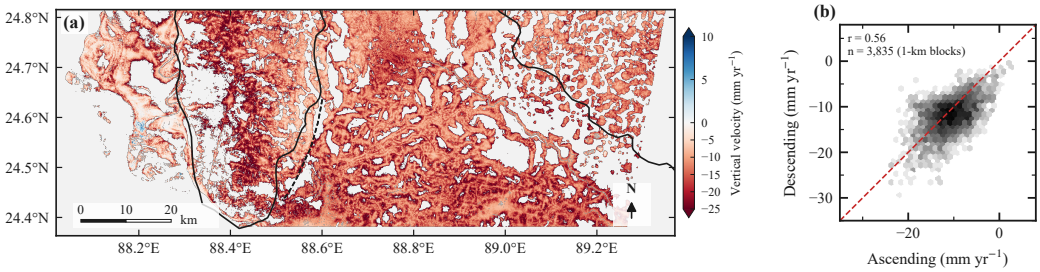


Figure 5: (a) Descending-track vertical velocity over the area covered by both tracks. (b) Ascending vs descending vertical velocity for 1-km block medians; dashed line is 1:1.

no clear acceleration or deceleration, which is consistent with continuing inelastic compaction rather than a transient response.

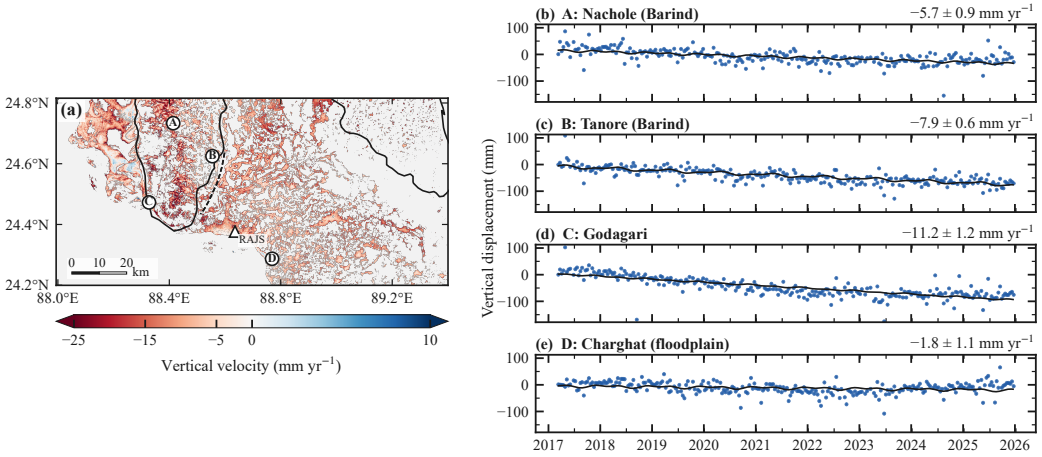


Figure 6: (a) Location of time-series sites A–D on the ascending velocity map. (b–e) GNSS-tied vertical displacement (1-km median of coherent pixels) with the harmonic-plus-trend fit (Eq. 1); rates with HAC standard errors.

GLDAS-2.2 groundwater storage over the study area declined by -7.2 ± 1.2 mm yr^{-1} and GRACE/GRACE-FO total water storage by -3.6 ± 1.5 mm yr^{-1} over the full record (Fig. 7a). Groundwater storage reaches its seasonal minimum in April, at the end of the Boro irrigation season, and recovers during the monsoon. The mean seasonal cycle of ground displacement reaches its minimum three to four months later (Fig. 7b): the fitted seasonal lows fall between late July and late August at all four sites (Nachole 30 July, Godagari 3 August, Charghat 19 August, Tanore 29 August), with peak-to-trough amplitudes of 6–12 mm. The pixel-wise timing map (Fig. S6) shows summer lows over most of the Barind Tract, whereas patches of the central floodplain reach their low in March–April, close to the groundwater minimum. Detrended month-by-month correlation between ground displacement and groundwater storage is weak ($|r| \leq 0.22$ at lags of -3 to $+4$ months), because the seasonal ground signal is small relative to epoch-to-epoch noise; the timing argument therefore rests on the fitted harmonic phases rather than on the correlation. The ERA5 correction leaves this picture essentially unchanged: over the 171 epochs it changed vertical velocities by a median of 0.03 mm yr^{-1} (95th percentile 0.29 mm yr^{-1}; $r = 1.000$), did not reduce time-series scatter, and moved the seasonal low at Nachole, Tanore and Charghat by only one to three weeks, keeping it in late August to early September (these test series are not refer-

enced to RAJS, so their timing differs slightly from Fig. 7b). Across all coherent pixels, the share with a July–September low increased from 26% to 35% after correction. At Godagari, where the seasonal amplitude is smallest (5–7 mm), the timing is not robust.

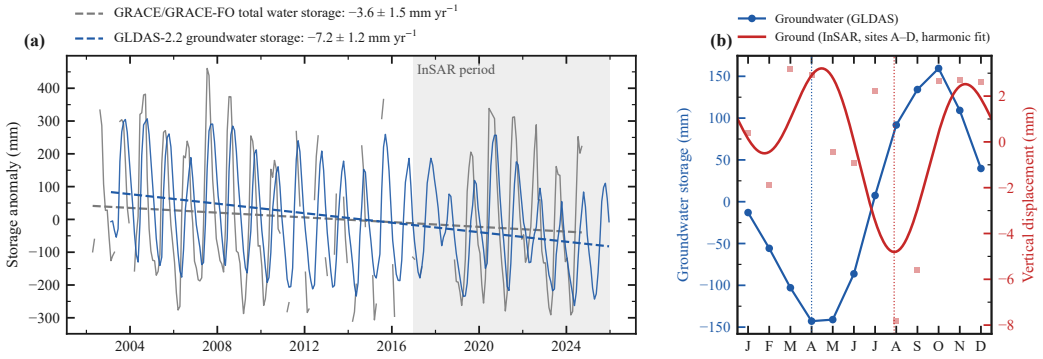


Figure 7: (a) GRACE/GRACE-FO total water storage and GLDAS-2.2 groundwater storage anomalies over the study area with HAC trends; shading marks the InSAR period. (b) Mean seasonal cycle of groundwater storage (2017–2025) and of InSAR vertical displacement at sites A–D (harmonic fit; squares are monthly means); dotted lines mark the minima.

4.4. Subsidence by geology and irrigation

Boro rice is concentrated on the eastern floodplains and the central Barind Tract (Fig. 8). Subsidence differs between geological units (Fig. 9). In the ascending track, Barind clay residuum (539 km^2 coherent) has a median of -11.7 mm yr^{-1} and 58% of its area subsides faster than 10 mm yr^{-1}, marsh clay and peat -11.0 mm yr^{-1} (58%), alluvial silt and clay -10.8 mm yr^{-1} (56%) and alluvial silt -9.4 mm yr^{-1} (46%), while alluvial sand on the active Ganges floodplain subsides least (-7.0 mm yr^{-1}, 34%). The descending track shows the same contrast between the Barind clay and the floodplain sand. By physiographic unit, the Barind Tract has the fastest median (-12.0 mm yr^{-1}, 5th percentile -27.2 mm yr^{-1}), followed by the Atrai floodplain (-11.6 mm yr^{-1}) and the Ganges floodplain (-8.4 mm yr^{-1}). The geology term of the reduced model has a mean SHAP contribution of -1.0 mm yr^{-1} on the Barind clay and $+1.3$ mm yr^{-1} on floodplain sand.

4.5. Model performance

Under 5-km spatial block cross-validation, the random forest explains R^2 = 0.37 of the ascending and 0.47 of the descending velocity (Table 3, Fig. 10).

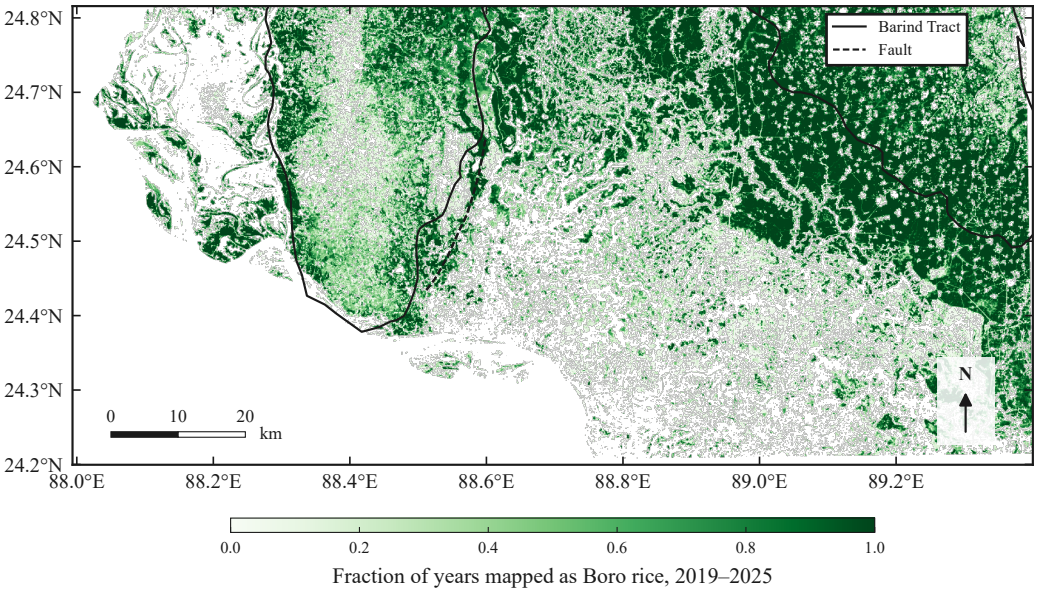


Figure 8: Fraction of years 2019–2025 mapped as Boro rice from Sentinel-2.

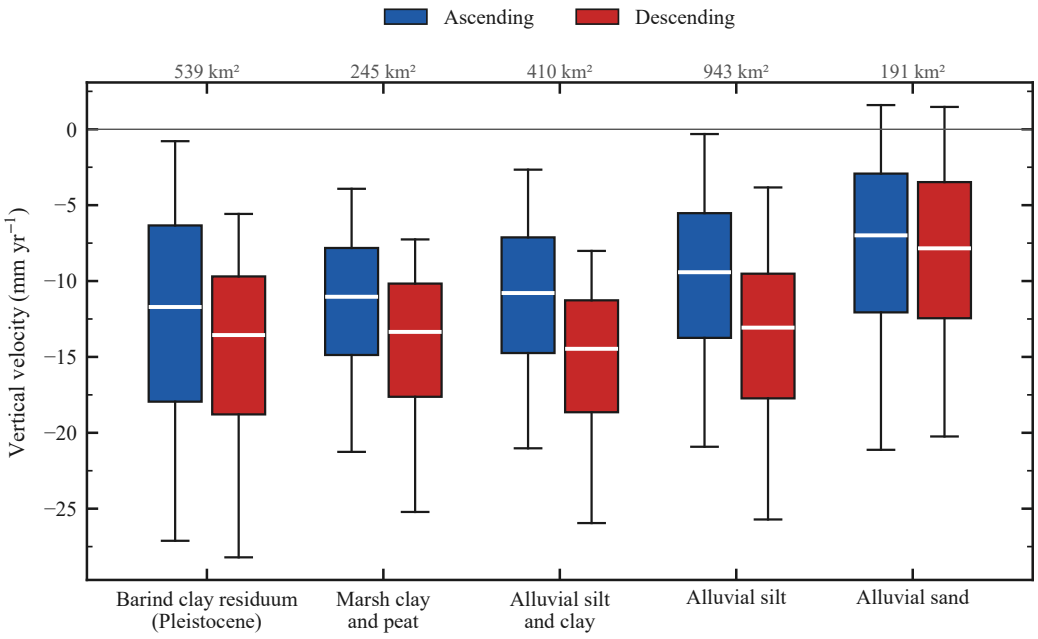


Figure 9: Vertical velocity by geological unit for both tracks. Boxes span the interquartile range, whiskers the 5th–95th percentiles; numbers give the coherent area.

Random cross-validation gives R^2 = 0.50 and 0.56, inflating apparent skill by 0.09–0.13. XGBoost performs almost identically to the random forest, and both outperform the linear baseline (R^2 = 0.19 spatial), indicating nonlinear effects. Larger 10-km blocks reduce spatial skill to 0.29, as expected when the model must extrapolate further. Without ramp removal, R^2 rises to 0.69 (spatial) and 0.76 (random): the model learns the long-wavelength artefact from smooth predictors such as rainfall and land-surface temperature, which shows that high skill can reflect processing artefacts rather than physical drivers. Moran's I of the observed velocity is 0.33–0.35 at 0–1 km and still 0.08–0.11 at 5–10 km; residuals retain short-range dependence (0.17–0.18 at 0–1 km) but $I \leq 0.01$ beyond the 5-km block size in both tracks (Fig. S5), confirming that the block design removes most dependence between folds.

Table 3: Cross-validated R^2 of random forest (RF) and XGBoost (XGB) under spatial (5-km block) and random five-fold cross-validation.

	Spatial CV		Random CV	
Experiment	RF	XGB	RF	XGB
All predictors (ascending)	0.37	0.36	0.50	0.50
Reduced predictor set	0.35	0.34	0.48	0.48
Coherence ≥ 0.5	0.41	0.41	0.51	0.52
10-km blocks	0.29	0.27	0.50	0.50
Descending track	0.47	0.47	0.56	0.57
No ramp removal (artefact)	0.69	0.68	0.76	0.76
Linear baseline, all predictors	0.19		0.21	

4.6. Drivers of the spatial pattern

Eight predictors have the same SHAP direction in both tracks (Fig. 11). Built-up share of the pixel and elevation have the largest mean absolute SHAP values (1.5–2.0 and 1.0–1.4 mm yr^{-1}): built-up pixels and higher ground subside less. Built-up share within 3 km has the opposite effect (more subsidence), as do local Boro frequency (pixel and 1 km) and distance to rivers. Relative relief and built-up share within 1 km are associated with less subsidence. Boro frequency at 3 and 5 km and all soil-texture variables change direction between tracks and are therefore not interpreted. Partial-dependence curves (Fig. 12) are similar for both tracks for the robust predictors.

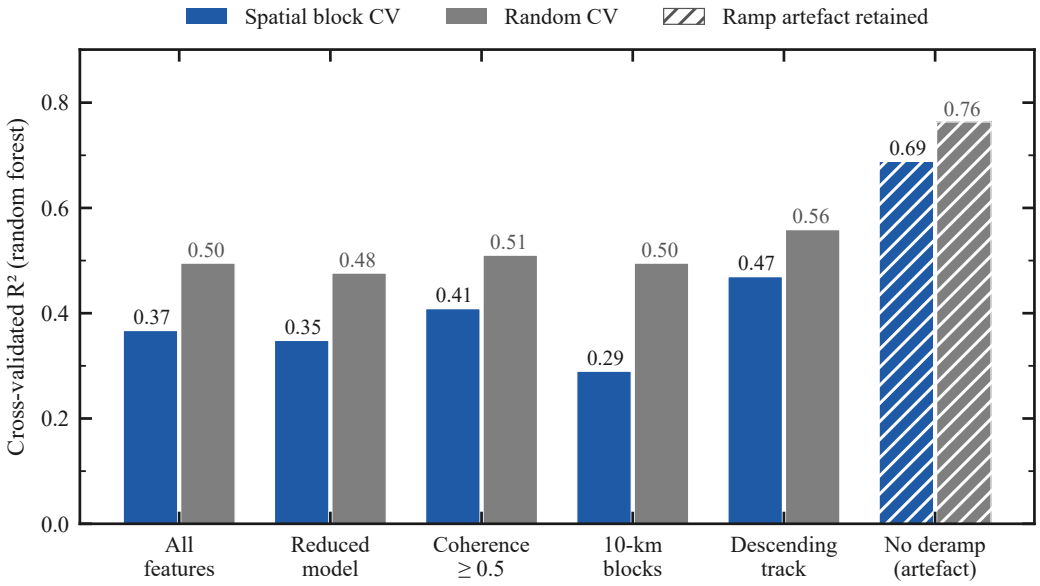


Figure 10: Spatial vs random cross-validated R^2 of the random forest for all experiments. Hatched bars: velocity field without ramp removal.

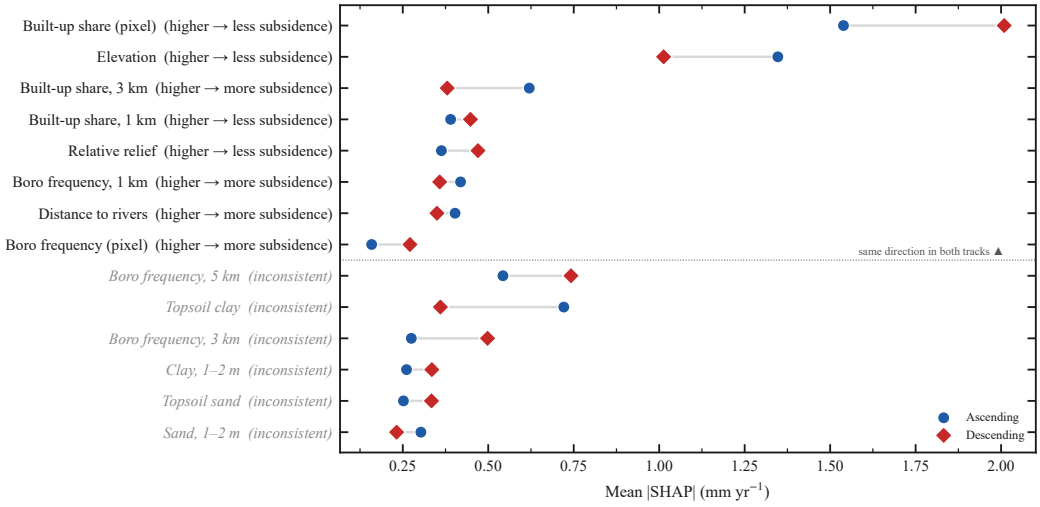


Figure 11: Mean absolute SHAP value of each predictor in the ascending and descending XGBoost models. Upper group: same direction of effect in both tracks (direction given in brackets); lower group (grey, italic): direction differs between tracks.

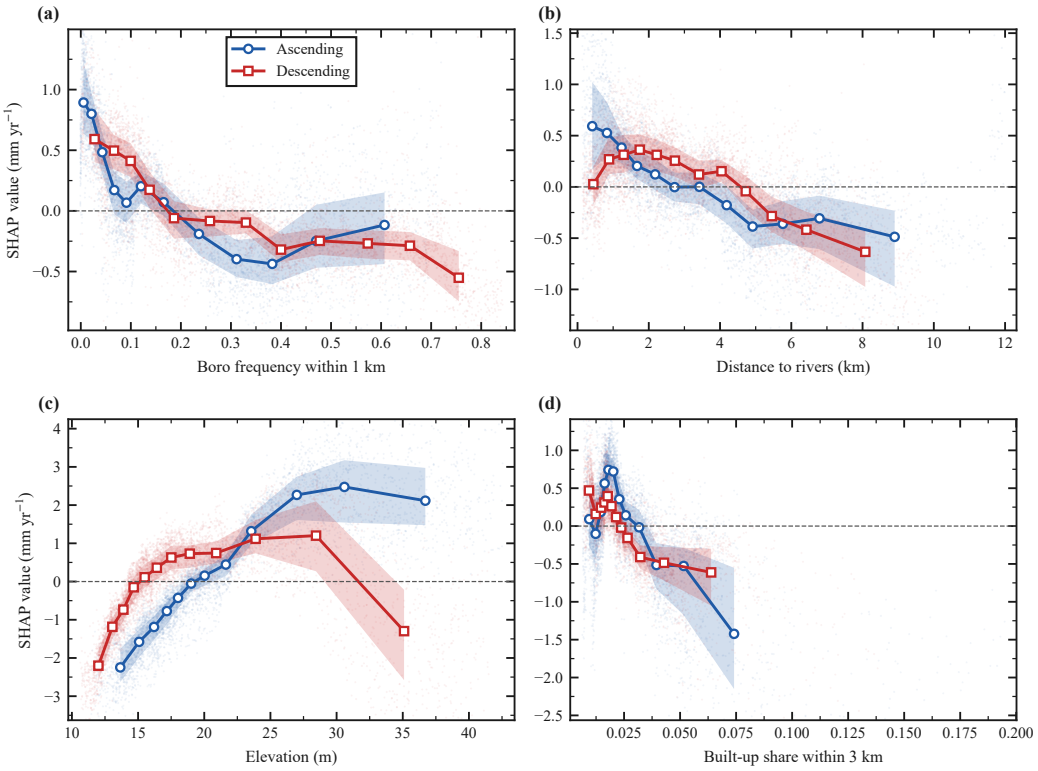


Figure 12: SHAP dependence of four robust predictors for both tracks: binned median (line) and interquartile range (band).

4.7. Volume loss and exposure

Subsidence of the 2243 km^2 of coherent subsiding land removes 25.2 ± 3.8 million m^3 of ground volume per year (222 million m^3 over 2017–2025), split between the Ganges floodplain (10.1 million m^3 yr^{-1}), the Atrai floodplain (8.2) and the Barind Tract (6.9). If non-coherent land subsides at the coherent median, the total for the 7597 km^2 of Bangladesh land in the frame rises to 77 million m^3 yr^{-1}. For comparison, the GLDAS groundwater-storage decline of 7.2 mm yr^{-1} over the same land corresponds to 55 million m^3 yr^{-1} of water. Exposure is uneven (Table 4): Boro cropland subsides faster than the area as a whole (median -12.4 mm yr^{-1}; 64% faster than 10 mm yr^{-1}), whereas built-up land is nearly stable (median -2.8 mm yr^{-1}; 4%). Of the 1359 km of main roads with InSAR measurements, 601 km (44%) lie on ground subsiding faster than 10 mm yr^{-1}, as do 101 km (54%) of the 186 km of measured railway.

Table 4: Exposure of land and transport infrastructure to subsidence faster than 10 mm yr^{-1} (ascending track, coherent pixels). Road length is that falling within the Bangladesh part of the frame; "measured" is the length with a coherent pixel within 80 m.

	Total	Measured	Median velocity (mm yr^{-1})	>10 mm yr^{-1}
All coherent land	–	2327 km^2	−10.1	1181 km^2 (51%)
Boro cropland	–	239 km^2	−12.4	154 km^2 (64%)
Built-up land	–	28 km^2	−2.8	1 km^2 (4%)
National highways	578 km	433 km	−8.5	181 km (42%)
Regional roads	545 km	348 km	−7.9	140 km (40%)
District and feeder roads	789 km	578 km	−9.7	280 km (48%)
Railways	233 km	186 km	−10.9	101 km (54%)

5. Discussion

5.1. Mechanism: compaction of the Barind clays by irrigation pumping

Three lines of evidence point to aquifer-system compaction driven by groundwater abstraction. First, the regional groundwater-storage decline of -7.2 mm yr^{-1} (cf. Shamsudduha et al., 2012; Rodell et al., 2009) coincides with persistent subsidence of up to -11 mm yr^{-1} at the Barind margin, a ratio of the same order as reported for compacting alluvial basins (Smith et al., 2017; Ojha et al., 2018). Second, subsidence is fastest on the clay-rich Barind residuum and slowest on the

sandy Ganges floodplain, as expected if fine-grained layers compact while sands deform mainly elastically (Galloway and Burbey, 2011). Third, the ground's seasonal low (late July–August) lags the groundwater-storage minimum (April) by three to four months at all four sites, whereas parts of the central floodplain reach their low in March–April. A lag of this size is typical of delayed drainage of thick aquitards (Smith et al., 2017; Haghshenas Haghighi and Motagh, 2019). It is, however, close to the monsoon peak, when wet-troposphere delay and soil swelling are largest. An ERA5 correction, however, did not remove or shift the summer low (it moved by one to three weeks and kept a similar amplitude), and the spatial variation of the timing (Fig. S6) also argues against a purely atmospheric origin, which would be more uniform across a 140-km frame. Turbulent water vapour below the ERA5 resolution and soil swelling cannot be excluded. Without piezometric data from the deep Barind aquifers, these inferences remain indirect; borehole extensometers or co-located piezometers would provide a definitive test.

5.2. Comparison with previous studies

Our results agree with the two earlier Sentinel-1 observations in the region. The line-of-sight rate of 8 mm yr^{-1} reported for Rajshahi by Middleton et al. (2025) corresponds to about 10 mm yr^{-1} vertically at a 39° incidence angle, matching our median of -10.1 mm yr^{-1}, and the 2–6 month lag of subsidence behind groundwater storage found nationally by Ouyang et al. (2024) brackets the three-to-four-month lag at our four sites. Our rates are also similar to those reported for groundwater-driven subsidence in the Indian Ganga plain (Raju et al., 2022; More et al., 2025). The measured Barind rates are comparable to the higher rates reported for the lower GBM delta (Higgins et al., 2014; Steckler et al., 2022, 2024), although the mechanism differs. Delta-plain subsidence is dominated by natural compaction of thick Holocene muds, whereas the Barind Tract has thin Holocene cover and its subsidence is more plausibly anthropogenic. Inland subsidence of this magnitude has received little attention in Bangladesh subsidence assessments, which focus on coastal flood risk; on the Barind it matters mainly for irrigation infrastructure, rural roads and the long-term storage capacity of the aquifer (Hasan et al., 2023).

5.3. What the attribution models do and do not show

The attribution models explain about a third of the spatial variance under spatial validation. This modest skill is realistic for a target that contains noise and for predictors that describe pumping only indirectly; it is consistent with the poor transferability reported for spatial ecological models (Ploton et al., 2020). Two

methodological results are general. First, random cross-validation overstated skill by 0.09–0.21 in R^2, in line with Roberts et al. (2017). Second, a velocity field with residual ramps produced the best-looking model of all ($R^2 = 0.69$), because smooth predictors such as rainfall and land-surface temperature can reproduce a planar artefact. High ML skill on InSAR targets therefore needs to be checked against processing choices before it is interpreted.

The robust predictors have plausible physical meanings but should be read as associations. Lower subsidence at higher elevation and on built-up pixels reflects, respectively, the thinner compressible cover on the dissected Barind uplands and the stability of buildings with shallow foundations as radar scatterers. Higher subsidence where built-up density within 3 km is high is consistent with concentrated municipal and industrial pumping around Rajshahi and the upazila towns. Local Boro frequency increases subsidence in both tracks, but the larger-scale Boro neighbourhood variables are inconsistent, probably because irrigation density at 3–5 km is collinear with geology and elevation (Fig. S4). The soil-texture variables come from 250-m SoilGrids predictions (Poggio et al., 2021) that describe only the upper 2 m and cannot represent the aquitards that actually compact, which explains their unstable SHAP directions.

5.4. Implications for groundwater management and infrastructure

The volume lost to subsidence (25–77 million $m^3\,yr^{-1}$) is of the same order as the regional groundwater-storage decline (55 million $m^3\,yr^{-1}$). If even part of the subsidence is inelastic compaction of the clay-rich Barind residuum and floodplain aquitards, a substantial fraction of the storage now being depleted may not be recoverable when pumping is reduced, as reported for other over-exploited alluvial aquifers (Smith et al., 2017; Hasan et al., 2023). Because part of the measured subsidence may come from shallow compaction unrelated to pumping, these numbers bound the hydrological loss from above and should be refined with extensometer or piezometer data. The faster subsidence of Boro cropland and the stability of built-up pixels are consistent with the SHAP attribution and point to irrigation pumping rather than building load as the dominant driver. Differential settlement of 8–11 $mm\,yr^{-1}$ along highways and railway embankments is modest per year but accumulates to 7–10 cm per decade, which matters for drainage gradients, bridge approaches and flood embankments on a floodplain only a few metres above river level.

6. Conclusions

A systematic review of 100 studies showed that InSAR work in Bangladesh has focused on Dhaka, the coast and a few point locations, leaving the inland Barind Tract, despite its well-documented groundwater depletion, without a spatially complete geodetic map, and that ML attributions of subsidence are rarely validated spatially. Using two independent Sentinel-1 tracks tied to GNSS, we find that:

1. most of the coherent area is subsiding, with a median of -10.1 mm yr^{-1} and rates of -8 to -11 mm yr^{-1} on the Barind margin, against about -2 mm yr^{-1} on the active Ganges floodplain;
2. subsidence is fastest on the Barind clay residuum and slowest on floodplain sands, and its seasonal low lags the groundwater-storage low by three to four months, consistent with delayed aquitard compaction;
3. random cross-validation and residual orbital ramps can each inflate ML skill substantially, so spatial block validation and processing sensitivity tests are essential;
4. only predictors with consistent SHAP directions in both tracks (elevation, built-up density, local Boro intensity, relief and distance to rivers) should be interpreted, while soil-texture effects are unstable;
5. subsidence removes 25–77 million m^3 of ground volume per year, comparable to the regional groundwater-storage decline, and affects about 600 km of main roads and 100 km of railway, while built-up land is nearly stable.

These results establish a baseline for monitoring the Barind aquifer and support co-locating piezometers and GNSS stations with the subsidence hotspots identified here.

Data availability

Sentinel-1 data are available from the Alaska Satellite Facility; official Boro statistics from the Bangladesh Bureau of Statistics (Bangladesh Bureau of Statistics, 2023); Sentinel-2, CHIRPS, SoilGrids, WorldCover, JRC GSW and MODIS from Google Earth Engine; GRACE/GRACE-FO mascons from NASA JPL; GLDAS-2.2 from NASA GES DISC; GNSS time series from the Nevada Geodetic Laboratory; geology from USGS Open-File Report 97-470-H. Processing scripts and derived velocity grids are available from the corresponding author on reasonable request and will be deposited in a public repository (Zenodo) on publication. Supplementary material (Figs. S1–S6, Table S1 literature-screening records and

Table S2) is available from Zenodo at https://doi.org/10.5281/zenodo.24145526.

CRediT authorship contribution statement

Farheen Zaman: Conceptualization, Methodology, Software, Formal analysis, Investigation, Data curation, Validation, Visualization, Writing – original draft, Writing – review & editing. **Ashfaq Raveed:** Conceptualization, Methodology, Software, Formal analysis, Investigation, Data curation, Validation, Visualization, Writing – original draft, Writing – review & editing. Both authors contributed equally to this work.

Declaration of competing interest

The authors declare no known competing financial interests or personal relationships that could have appeared to influence the work reported in this paper.

Acknowledgements

We thank ASF for HyP3 processing, the MintPy developers, and the Nevada Geodetic Laboratory for GNSS solutions.

References

Alaska Satellite Facility, 2025. HyP3: Hybrid Pluggable Processing Pipeline, Sentinel-1 InSAR (GAMMA) on-demand products. https://hyp3-docs.asf.alaska.edu/. Accessed 2025.

Ao, Z., Hu, X., Tao, S., Hu, X., Wang, G., Li, M., et al., 2024. A national-scale assessment of land subsidence in China's major cities. Science 384, 301–306. doi:10.1126/science.adl4366.

Bagheri-Gavkosh, M., Hosseini, S.M., Ataie-Ashtiani, B., Sohani, Y., Ebrahimian, H., Morovat, F., Ashrafi, S., 2021. Land subsidence: A global challenge. Science of The Total Environment 778, 146193. doi:10.1016/j.scitotenv.2021.146193.

Bangladesh Bureau of Statistics, 2023. Yearbook of Agricultural Statistics-2022 (34th Series). Statistics and Informatics Division, Ministry of Planning, Government of the People's Republic of Bangladesh, Dhaka.

Becker, M., Papa, F., Karpytchev, M., Delebecque, C., Krien, Y., Khan, J.U., et al., 2020. Water level changes, subsidence, and sea level rise in the Ganges–Brahmaputra–Meghna delta. Proceedings of the National Academy of Sciences 117, 1867–1876. doi:10.1073/pnas.1912921117.

Berardino, P., Fornaro, G., Lanari, R., Sansosti, E., 2002. A new algorithm for surface deformation monitoring based on small baseline differential SAR interferograms. IEEE Transactions on Geoscience and Remote Sensing 40, 2375–2383. doi:10.1109/TGRS.2002.803792.

Blewitt, G., Hammond, W.C., Kreemer, C., 2018. Harnessing the GPS data explosion for interdisciplinary science. Eos 99. doi:10.1029/2018EO104623.

Brammer, H., 2012. The Physical Geography of Bangladesh. The University Press Limited, Dhaka.

Breiman, L., 2001. Random forests. Machine Learning 45, 5–32. doi:10.1023/A:1010933404324.

Brown, S., Nicholls, R.J., 2015. Subsidence and human influences in mega deltas: The case of the Ganges–Brahmaputra–Meghna. Science of The Total Environment 527–528, 362–374. doi:10.1016/j.scitotenv.2015.04.124.

Castellazzi, P., Martel, R., Rivera, A., Huang, J., Pavlic, G., Calderhead, A.I., Chaussard, E., Garfias, J., Salas, J., 2016. Groundwater depletion in Central Mexico: Use of GRACE and InSAR to support water resources management. Water Resources Research 52, 5985–6003. doi:10.1002/2015WR018211.

Chaussard, E., Amelung, F., Abidin, H., Hong, S.H., 2013. Sinking cities in Indonesia: ALOS PALSAR detects rapid subsidence due to groundwater and gas extraction. Remote Sensing of Environment 128, 150–161. doi:10.1016/j.rse.2012.10.015.

Chaussard, E., Wdowinski, S., Cabral-Cano, E., Amelung, F., 2014. Land subsidence in central Mexico detected by ALOS InSAR time-series. Remote Sensing of Environment 140, 94–106. doi:10.1016/j.rse.2013.08.038.

Chen, T., Guestrin, C., 2016. XGBoost: A scalable tree boosting system, in: Proceedings of the 22nd ACM SIGKDD International Conference on Knowledge Discovery and Data Mining, pp. 785–794. doi:10.1145/2939672.2939785.

Davydzenka, T., Tahmasebi, P., Shokri, N., 2024. Unveiling the global extent of land subsidence: The sinking crisis. Geophysical Research Letters 51, e2023GL104497. doi:10.1029/2023GL104497.

Dey, N.C., Saha, R., Parvez, M., Bala, S.K., Islam, A.K.M.S., Paul, J.K., Hossain, M., 2017. Sustainability of groundwater use for irrigation of dry-season crops in northwest Bangladesh. Groundwater for Sustainable Development 4, 66–77. doi:10.1016/j.gsd.2017.02.001.

Dong, J., Xiao, X., 2016. Evolution of regional to global paddy rice mapping methods: A review. ISPRS Journal of Photogrammetry and Remote Sensing 119, 214–227. doi:10.1016/j.isprsjprs.2016.05.010.

Drusch, M., Del Bello, U., Carlier, S., Colin, O., Fernandez, V., Gascon, F., et al., 2012. Sentinel-2: ESA's optical high-resolution mission for GMES operational services. Remote Sensing of Environment 120, 25–36. doi:10.1016/j.rse.2011.11.026.

Erban, L.E., Gorelick, S.M., Zebker, H.A., 2014. Groundwater extraction, land subsidence, and sea-level rise in the Mekong Delta, Vietnam. Environmental Research Letters 9, 084010. doi:10.1088/1748-9326/9/8/084010.

Fattahi, H., Amelung, F., 2013. DEM error correction in InSAR time series. IEEE Transactions on Geoscience and Remote Sensing 51, 4249–4259. doi:10.1109/TGRS.2012.2227761.

Ferretti, A., Prati, C., Rocca, F., 2001. Permanent scatterers in SAR interferometry. IEEE Transactions on Geoscience and Remote Sensing 39, 8–20. doi:10.1109/36.898661.

Fuhrmann, T., Garthwaite, M.C., 2019. Resolving three-dimensional surface motion with InSAR: Constraints from multi-geometry data fusion. Remote Sensing 11, 241. doi:10.3390/rs11030241.

Funk, C., Peterson, P., Landsfeld, M., Pedreros, D., Verdin, J., Shukla, S., et al., 2015. The climate hazards infrared precipitation with stations—a new environmental record for monitoring extremes. Scientific Data 2, 150066. doi:10.1038/sdata.2015.66.

Galloway, D.L., Burbey, T.J., 2011. Review: Regional land subsidence accompanying groundwater extraction. Hydrogeology Journal 19, 1459–1486. doi:10.1007/s10040-011-0775-5.

Goodbred, S.L., Kuehl, S.A., 2000. The significance of large sediment supply, active tectonism, and eustasy on margin sequence development: Late Quaternary stratigraphy and evolution of the Ganges–Brahmaputra delta. Sedimentary Geology 133, 227–248. doi:10.1016/S0037-0738(00)00041-5.

Gorelick, N., Hancher, M., Dixon, M., Ilyushchenko, S., Thau, D., Moore, R., 2017. Google Earth Engine: Planetary-scale geospatial analysis for everyone. Remote Sensing of Environment 202, 18–27. doi:10.1016/j.rse.2017.06.031.

Grall, C., Steckler, M.S., Pickering, J.L., Goodbred, S., Sincavage, R., Paola, C., Akhter, S.H., Spiess, V., 2018. A base-level stratigraphic approach to determining Holocene subsidence of the Ganges–Meghna–Brahmaputra delta plain. Earth and Planetary Science Letters 488, 120–131. doi:10.1016/j.epsl.2018.02.013.

Haghshenas Haghighi, M., Motagh, M., 2019. Ground surface response to continuous compaction of aquifer system in Tehran, Iran: Results from a long-term multi-sensor InSAR analysis. Remote Sensing of Environment 221, 534–550. doi:10.1016/j.rse.2018.11.003.

Hasan, M.F., Smith, R., Vajedian, S., Pommerenke, R., Majumdar, S., 2023. Global land subsidence mapping reveals widespread loss of aquifer storage capacity. Nature Communications 14, 6180. doi:10.1038/s41467-023-41933-z.

Herrera-García, G., Ezquerro, P., Tomás, R., Béjar-Pizarro, M., López-Vinielles, J., Rossi, M., Mateos, R.M., Carreón-Freyre, D., Lambert, J., Teatini, P., et al., 2021. Mapping the global threat of land subsidence. Science 371, 34–36. doi:10.1126/science.abb8549.

Higgins, S.A., Overeem, I., Steckler, M.S., Syvitski, J.P.M., Seeber, L., Akhter, S.H., 2014. InSAR measurements of compaction and subsidence in the Ganges-Brahmaputra Delta, Bangladesh. Journal of Geophysical Research: Earth Surface 119, 1768–1781. doi:10.1002/2014JF003117.

Huang, Z.h., Huo, Z.b., Wang, W., Zhu, J.x., Zhang, C.h., Xi, R.p., 2025. Analysis of driving factors for land subsidence in typical cities of the North China

Plain based on geodetector technology. Journal of Groundwater Science and Engineering 13, 74–89. doi:10.26599/JGSE.2025.9280040.

Jahan, C.S., Mazumder, Q.H., Islam, A.T.M.M., Adham, M.I., 2010. Impact of irrigation in Barind area, NW Bangladesh—an evaluation based on the meteorological parameters and fluctuation trend in groundwater table. Journal of the Geological Society of India 76, 134–142. doi:10.1007/s12594-010-0085-1.

Jolivet, R., Grandin, R., Lasserre, C., Doin, M.P., Peltzer, G., 2011. Systematic InSAR tropospheric phase delay corrections from global meteorological reanalysis data. Geophysical Research Letters 38, L17311. doi:10.1029/2011GL048757.

Khan, N.S., Xie, S., 2025. Accelerated land subsidence and complex temporal variations in newly developed areas in Dhaka, Bangladesh, observed by InSAR. IEEE Geoscience and Remote Sensing Letters 22, 3001305. doi:10.1109/LGRS.2025.3536996.

Kumar, H., Syed, T.H., Amelung, F., Agrawal, R., Venkatesh, A.S., 2022. Space-time evolution of land subsidence in the National Capital Region of India using ALOS-1 and Sentinel-1 SAR data: Evidence for groundwater overexploitation. Journal of Hydrology 605, 127329. doi:10.1016/j.jhydrol.2021.127329.

Kyaw, K.M., Takeuchi, W., 2025. Instability mapping of Dhaka-Kasiani-Gopalganj railway line in Bangladesh with InSAR time series analysis. Scientific Reports 15, 37449. doi:10.1038/s41598-025-21375-x.

Landerer, F.W., Flechtner, F.M., Save, H., Webb, F.H., Bandikova, T., Bertiger, W.I., et al., 2020. Extending the global mass change data record: GRACE Follow-On instrument and science data performance. Geophysical Research Letters 47, e2020GL088306. doi:10.1029/2020GL088306.

Li, B., Rodell, M., Kumar, S., Beaudoing, H.K., Getirana, A., Zaitchik, B.F., et al., 2019. Global GRACE data assimilation for groundwater and drought monitoring: Advances and challenges. Water Resources Research 55, 7564–7586. doi:10.1029/2018WR024618.

Lundberg, S.M., Erion, G., Chen, H., DeGrave, A., Prutkin, J.M., Nair, B., Katz, R., Himmelfarb, J., Bansal, N., Lee, S.I., 2020. From local explanations to global understanding with explainable AI for trees. Nature Machine Intelligence 2, 56–67. doi:10.1038/s42256-019-0138-9.

Lundberg, S.M., Lee, S.I., 2017. A unified approach to interpreting model predictions, in: Advances in Neural Information Processing Systems 30, pp. 4765–4774.

Meyer, H., Pebesma, E., 2021. Predicting into unknown space? Estimating the area of applicability of spatial prediction models. Methods in Ecology and Evolution 12, 1620–1633. doi:10.1111/2041-210X.13650.

Middleton, G.D., Gani, N.D., Gani, M.R., 2025. Advancing geohazard monitoring: Sentinel-1 InSAR observations of land subsidence in northern and central Bangladesh. Geological Journal 60, 1106–1128. doi:10.1002/gj.5206.

Minderhoud, P.S.J., Erkens, G., Pham, V.H., Bui, V.T., Erban, L., Kooi, H., Stouthamer, E., 2017. Impacts of 25 years of groundwater extraction on subsidence in the Mekong delta, Vietnam. Environmental Research Letters 12, 064006. doi:10.1088/1748-9326/aa7146.

Mohammady, M., Pourghasemi, H.R., Amiri, M., 2019. Land subsidence susceptibility assessment using random forest machine learning algorithm. Environmental Earth Sciences 78, 503. doi:10.1007/s12665-019-8518-3.

Mojid, M.A., Parvez, M.F., Mainuddin, M., Hodgson, G., 2019. Water table trend—a sustainability status of groundwater development in North-West Bangladesh. Water 11, 1182. doi:10.3390/w11061182.

Moran, P.A.P., 1950. Notes on continuous stochastic phenomena. Biometrika 37, 17–23. doi:10.2307/2332142.

More, S., Tiwari, V.M., Tiwari, A., Ravikumar, M., 2025. Groundwater overextraction and associated land subsidence in Lucknow, Ganga basin, India: Insights from space geodetic observations. Near Surface Geophysics 23, 420–433. doi:10.1002/nsg.70020.

Morgan, J.P., McIntire, W.G., 1959. Quaternary geology of the Bengal Basin, East Pakistan and India. Geological Society of America Bulletin 70, 319–342. doi:10.1130/0016-7606(1959)70[319:QGOTBB]2.0.CO;2.

Newey, W.K., West, K.D., 1987. A simple, positive semi-definite, heteroskedasticity and autocorrelation consistent covariance matrix. Econometrica 55, 703–708. doi:10.2307/1913610.

Ohenhen, L.O., Shirzaei, M., Ojha, C., Sherpa, S.F., Nicholls, R.J., 2024. Disappearing cities on US coasts. Nature 627, 108–115. doi:10.1038/s41586-024-07038-3.

Ojha, C., Shirzaei, M., Werth, S., Argus, D.F., Farr, T.G., 2018. Sustained groundwater loss in California's Central Valley exacerbated by intense drought periods. Water Resources Research 54, 4449–4460. doi:10.1029/2017WR022250.

OpenStreetMap contributors, 2026. OpenStreetMap. Planet dump retrieved via the Overpass API, https://www.openstreetmap.org. Accessed 7 November 2026.

Ouyang, L., Zhao, Z., Zhou, D., Cao, J., Qin, J., Cao, Y., He, Y., 2024. Study on the relationship between groundwater and land subsidence in Bangladesh combining GRACE and InSAR. Remote Sensing 16, 3715. doi:10.3390/rs16193715.

Page, M.J., McKenzie, J.E., Bossuyt, P.M., Boutron, I., Hoffmann, T.C., Mulrow, C.D., et al., 2021. The PRISMA 2020 statement: an updated guideline for reporting systematic reviews. BMJ 372, n71. doi:10.1136/bmj.n71.

Pekel, J.F., Cottam, A., Gorelick, N., Belward, A.S., 2016. High-resolution mapping of global surface water and its long-term changes. Nature 540, 418–422. doi:10.1038/nature20584.

Persits, F.M., Wandrey, C.J., Milici, R.C., Manwar, A., 2001. Maps showing geology, oil and gas fields and geologic provinces of Bangladesh. Open-File Report 97-470-H. U.S. Geological Survey. doi:10.3133/ofr97470H.

Ploton, P., Mortier, F., Réjou-Méchain, M., Barbier, N., Picard, N., Rossi, V., et al., 2020. Spatial validation reveals poor predictive performance of large-scale ecological mapping models. Nature Communications 11, 4540. doi:10.1038/s41467-020-18321-y.

Poggio, L., de Sousa, L.M., Batjes, N.H., Heuvelink, G.B.M., Kempen, B., Ribeiro, E., Rossiter, D., 2021. SoilGrids 2.0: producing soil information for the globe with quantified spatial uncertainty. SOIL 7, 217–240. doi:10.5194/soil-7-217-2021.

Qureshi, A.S., Ahmed, Z.U., Krupnik, T.J., 2015. Moving from resource development to resource management: Problems, prospects and policy recommendations for sustainable groundwater management in Bangladesh. Water Resources Management 29, 4269–4283. doi:10.1007/s11269-015-1059-y.

Rahman, M.M., Mahbub, A.Q.M., 2012. Groundwater depletion with expansion of irrigation in Barind Tract: A case study of Tanore Upazila. Journal of Water Resource and Protection 4, 567–575. doi:10.4236/jwarp.2012.48066.

Raju, A., Nanda, R., Singh, A., Malik, K., 2022. Multi-temporal analysis of groundwater depletion-induced land subsidence in Central Ganga alluvial plain, northern India. Geocarto International 37, 11732–11755. doi:10.1080/10106049.2022.2060322.

Roberts, D.R., Bahn, V., Ciuti, S., Boyce, M.S., Elith, J., Guillera-Arroita, G., et al., 2017. Cross-validation strategies for data with temporal, spatial, hierarchical, or phylogenetic structure. Ecography 40, 913–929. doi:10.1111/ecog.02881.

Rodell, M., Famiglietti, J.S., Wiese, D.N., Reager, J.T., Beaudoing, H.K., Landerer, F.W., Lo, M.H., 2018. Emerging trends in global freshwater availability. Nature 557, 651–659. doi:10.1038/s41586-018-0123-1.

Rodell, M., Velicogna, I., Famiglietti, J.S., 2009. Satellite-based estimates of groundwater depletion in India. Nature 460, 999–1002. doi:10.1038/nature08238.

Sarker, M.S., Kamal, A.S.M.M., Rahman, M.Z., Faruki Fahim, A.K., 2024. Land subsidence monitoring using InSAR technique in the southwestern region of Bangladesh. Geomatics, Natural Hazards and Risk 15, 2333795. doi:10.1080/19475705.2024.2333795.

Sen, P.K., 1968. Estimates of the regression coefficient based on Kendall's tau. Journal of the American Statistical Association 63, 1379–1389. doi:10.1080/01621459.1968.10480934.

Shamsudduha, M., Chandler, R.E., Taylor, R.G., Ahmed, K.M., 2009. Recent trends in groundwater levels in a highly seasonal hydrological system: the Ganges-Brahmaputra-Meghna Delta. Hydrology and Earth System Sciences 13, 2373–2385. doi:10.5194/hess-13-2373-2009.

Shamsudduha, M., Taylor, R.G., Ahmed, K.M., Zahid, A., 2011. The impact of intensive groundwater abstraction on recharge to a shallow regional aquifer system: evidence from Bangladesh. Hydrogeology Journal 19, 901–916. doi:10.1007/s10040-011-0723-4.

Shamsudduha, M., Taylor, R.G., Longuevergne, L., 2012. Monitoring groundwater storage changes in the highly seasonal humid tropics: Validation of GRACE measurements in the Bengal Basin. Water Resources Research 48, W02508. doi:10.1029/2011WR010993.

Shi, L., Gong, H., Chen, B., Zhou, C., 2020. Land subsidence prediction induced by multiple factors using machine learning method. Remote Sensing 12, 4044. doi:10.3390/rs12244044.

Smith, R., Majumdar, S., 2020. Groundwater storage loss associated with land subsidence in western United States mapped using machine learning. Water Resources Research 56, e2019WR026621. doi:10.1029/2019WR026621.

Smith, R.G., Knight, R., Chen, J., Reeves, J.A., Zebker, H.A., Farr, T., Liu, Z., 2017. Estimating the permanent loss of groundwater storage in the southern San Joaquin Valley, California. Water Resources Research 53, 2133–2148. doi:10.1002/2016WR019861.

Steckler, M.S., Jaman, M.H., Grall, C.J., Goodbred, S.L., Wilson, C.A., Oryan, B., 2024. Contribution of campaign GNSS toward parsing subsidence rates by time and depth in coastal Bangladesh. Frontiers in Earth Science 12, 1354686. doi:10.3389/feart.2024.1354686.

Steckler, M.S., Oryan, B., Wilson, C.A., Grall, C., Nooner, S.L., Mondal, D.R., Akhter, S.H., DeWolf, S., Goodbred, S.L., 2022. Synthesis of the distribution of subsidence of the lower Ganges-Brahmaputra Delta, Bangladesh. Earth-Science Reviews 224, 103887. doi:10.1016/j.earscirev.2021.103887.

Syvitski, J.P.M., Kettner, A.J., Overeem, I., Hutton, E.W.H., Hannon, M.T., Brakenridge, G.R., et al., 2009. Sinking deltas due to human activities. Nature Geoscience 2, 681–686. doi:10.1038/ngeo629.

Tapley, B.D., Bettadpur, S., Ries, J.C., Thompson, P.F., Watkins, M.M., 2004. GRACE measurements of mass variability in the Earth system. Science 305, 503–505. doi:10.1126/science.1099192.

Tessler, Z.D., Vörösmarty, C.J., Grossberg, M., Gladkova, I., Aizenman, H., Syvitski, J.P.M., Foufoula-Georgiou, E., 2015. Profiling risk and sustainability in coastal deltas of the world. Science 349, 638–643. doi:10.1126/science.aab3574.

Torres, R., Snoeij, P., Geudtner, D., Bibby, D., Davidson, M., Attema, E., et al., 2012. GMES Sentinel-1 mission. Remote Sensing of Environment 120, 9–24. doi:10.1016/j.rse.2011.05.028.

Valavi, R., Elith, J., Lahoz-Monfort, J.J., Guillera-Arroita, G., 2019. blockCV: An r package for generating spatially or environmentally separated folds for k-fold cross-validation of species distribution models. Methods in Ecology and Evolution 10, 225–232. doi:10.1111/2041-210X.13107.

Wan, Z., Hook, S., Hulley, G., 2015. MOD11A2 MODIS/Terra land surface temperature/emissivity 8-day L3 global 1km SIN grid V006. doi:10.5067/MODIS/MOD11A2.006.

Watkins, M.M., Wiese, D.N., Yuan, D.N., Boening, C., Landerer, F.W., 2015. Improved methods for observing Earth's time variable mass distribution with GRACE using spherical cap mascons. Journal of Geophysical Research: Solid Earth 120, 2648–2671. doi:10.1002/2014JB011547.

Wright, T.J., Parsons, B.E., Lu, Z., 2004. Toward mapping surface deformation in three dimensions using InSAR. Geophysical Research Letters 31, L01607. doi:10.1029/2003GL018827.

Xiao, X., Boles, S., Liu, J., Zhuang, D., Frolking, S., Li, C., Salas, W., Moore, B., 2005. Mapping paddy rice agriculture in southern China using multi-temporal MODIS images. Remote Sensing of Environment 95, 480–492. doi:10.1016/j.rse.2004.12.009.

Yunjun, Z., Fattahi, H., Amelung, F., 2019. Small baseline InSAR time series analysis: Unwrapping error correction and noise reduction. Computers & Geosciences 133, 104331. doi:10.1016/j.cageo.2019.104331.

Zanaga, D., Van De Kerchove, R., De Keersmaecker, W., Souverijns, N., Brockmann, C., Quast, R., et al., 2021. ESA WorldCover 10 m 2020 v100. doi:10.5281/zenodo.5571936.

Zhao, R., Arabameri, A., Santosh, M., 2024. Land subsidence susceptibility mapping: a new approach to improve decision stump classification (DSC) performance and combine it with four machine learning algorithms. Environmental Science and Pollution Research 31, 15443–15466. doi:10.1007/s11356-024-32075-w.